Nonlinear Dyn (2019) 98:3125–3141
https://doi.org/10.1007/s11071-019-05364-0

ORIGINAL PAPER

Fractional techniques to characterize non-solid aluminum electrolytic capacitors for power electronic applications

Xi Chen · Lei Xi · Yunning Zhang · Hui Ma · Yuehua Huang · Yangquan Chen

Received: 15 December 2018 / Accepted: 12 November 2019 / Published online: 21 November 2019

Abstract Non-solid aluminum electrolytic capacitors are one type of reliability-critical components, and they are widely adopted in power electronic converters. The capacitance and equivalent series resistance of these components have significant effects on the performance and reliability of power electronic systems. In this work, by exploring the electrochemical principles of aluminum electrolytic capacitors, the fractional-order (FO) characteristics of the capacitors are revealed, according to which the frequency-dependent parameters of this kind of components are expressed by FO models, while the parameters of the models are estimated by a multi-objective optimization algorithm. Under the same conditions such as the number of arguments supplied and optimization algorithm, the proposed models perform better. Additionally, to show further applications of fractional techniques, a brief example on the output ripple analysis of DC–DC converters is offered, in which one of the proposed FO models of the capacitor is adopted. The effectiveness and superiority of the techniques for predicting the states of the converters are confirmed by comparison with traditional models.

Keywords Aluminum electrolytic capacitors · Fractional order (FO) · Multi-objective optimization algorithm · DC–DC converters

1 Introduction

For many power electronic applications, such as power supplies, filter applications, and snubber circuits, the performance and reliability have always been important issues [1–3]. In these applications, electrolytic capacitors, metallized polypropylene film capacitors, and multilayer ceramic capacitors are generally used as filtering or energy storage components, but aluminum electrolytic capacitors with non-solid electrolyte gain wider adoptions because of its superiority in capacitance per unit volume and cost performance [4].

As shown in Fig. 1, when a non-solid aluminum electrolytic capacitor is in charging or discharging state, a typical internal structure appears.

As depicted in Fig. 1, the anode electrode of an aluminum electrolytic capacitor is made of an aluminum foil, the surface of which is etched by optical and electrical procedures, and an infinite self-similar structure is formed then. This layer of anodization acts as the dielectric and plays an important role in determining the lifetime, permissible voltage, and capacitance of the capacitor [5]. The electrolyte, in this work it is non-

X. Chen (✉)· L. Xi · Y. Zhang · H. Ma · Y. Huang
College of Electrical Engineering and New Energy, China Three Gorges University, Yichang 443002, Hubei, China
e-mail: xichen_1021@hotmail.com

Y. Chen
School of Engineering, University of California, Merced, CA 95343, USA
e-mail: ychen53@ucmerced.edu

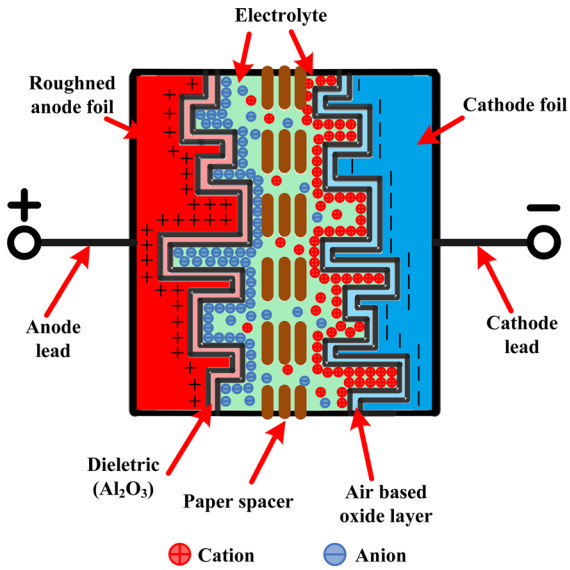

Fig. 1 Internal structure of non-solid aluminum electrolytic capacitor

solid, fills every available space inside the capacitor, serving as the cathode of the capacitor, while a second aluminum foil, which is usually called as cathode foil, is separated with the anode foil by a paper spacer and is used to collect charges of the cathode. On the surface of the cathode foil, there is a thick air- based oxide layer of aluminum [6]. Generally, the capacitance of electrolytic capacitors is depended on the applied potential between electrodes and the ionic concentration of electrolytes [7]. As a result, the variation in the applied potential and the vaporization of electrolytes will always lead to the value drift of the capacitors. Actually, many factors have short- or long-term impacts on these parameters [8]; thus, the electrolytic capacitor is one of the weakest links in power electronic circuits [9], the failures of which will further affect the performances of the circuits [10]. Accordingly, monitoring and predicting the conditions of this kind of components can provide guidance for the reliability design and analysis of power electronic systems [11], and a large number of scientific works have been published on these issues in the past few years [12].

In this work, to provide more accurate responses for the reliability design and characteristic analysis of power electronic systems, the concept of fractional impedance is introduced, which is utilized to construct the connection between electrical characteristics and electrochemical characteristics of non-solid aluminum electrolytic capacitors, while new fractional-order equivalent models are proposed, by which the frequency-related ESR and capacitance of the capacitors can be predicted. Additionally, to estimate the subspace parameters of the models, a multi-objective optimization scheme based on differential evolution algorithm is adopted. The practicability of the techniques is manifested in the voltage ripple analysis of DC–DC Boost converters.

The rest of the work is organized as follows: In Sect. 2, the electrochemical principles of aluminum electrolytic capacitors are presented, following which some traditional models for describing and specifying the capacitors are introduced, and the fractional-order equivalent models of the capacitors are constructed. Then, in Sect. 3, an implementation scenario for estimating the subspace parameters of the proposed models is offered. Moreover, comparisons of the predicting capacitance and ESR values between traditional models and the proposed models are presented in this section. Section 4 discusses the output voltage ripple of a DC–DC Boost converter based on the fractional-order model of non-solid aluminum electrolytic capacitor, in which the capacitor is usually used for filtering purpose. Finally, conclusions are outlined in Sect. 5.

2 Electrochemical principles and capacitor modeling

Ideal capacitor can be simply regarded as being composed of two metal sheets separated by a dielectric material. When an electric potential is applied, charge is transported through the electrodes by the movement of ions; therefore, an internal electric field is constructed, and mathematically, its behavior can be governed by:

$$C = \frac{q}{E}, \tag{1}$$

in which C is the capacitance, q is charge stored (in coulombs), and E is the potential (in volts).

On the other hand, the two electrodes with rough surface can be considered as two parallel plates of surface area S; thus, by Hermann von Helmholtz's definition of plate capacitors, the capacitance can be expressed by:

$$C = \frac{\varepsilon_r S}{4\pi kd}, \tag{2}$$

where ε_r is the permittivity of electrolyte, k is Boltzmann constant, and d is the thickness of the aforementioned aluminum oxide layer.

The above two equations describe the ideal situation; however, the electrode surface is not that smooth, and complex reactions appear in the electrolyte, which influence the electric field distribution and further affect the capacitance. Consequently, the above two models fail to deal with actual situations, and more precise model is required to better depict the characteristics of the capacitor.

2.1 Electrochemical principles and the double-layer model

When an aluminum electrolytic capacitor is in charging or discharging process, a typical double-layer structure appears in the capacitor. Specifically speaking, a compact layer or "Helmholtz layer" of ions is formed on the rough electrode surface, while an outer layer or "diffuse layer" of ions is formed in the electrolyte [7]. Under the joint effects of these two layers of ions, the capacitance of the capacitor can be governed by the following formula:

$$\begin{aligned}\frac{1}{C} &= \frac{4\pi kd}{\varepsilon_r S} + \frac{2GT}{FQ_T}\sinh^{-1}\left(\frac{Q_T}{\varepsilon_r A_v\sqrt{8GT\varepsilon_r c}}\right) \\ &= \frac{1}{C_{\text{Helmholtz}}} + \frac{1}{C_{\text{diffusion}}},\end{aligned} \tag{3}$$

in which G is the ideal gas constant per molecule, Q_T is the charge quantity, A_v is Avogadro's number, F is the Faraday constant, T is the temperature (in Kelvin), and c is the molar concentration of electrolyte.

This kind of double-layer structure is the result of the variation in electric potential near a surface, which can be regarded as two capacitors in series with each other. The model was developed by Louis Georges Gouy, David Leonard Chapman, and Otto Stern in the early 1900s [13], so it is also called as Gouy–Chapman–Stern model. According to its definition, the inner layer includes those specifically adsorbed ions, while the outer diffuse layer represents those solvated ones, or nonspecifically adsorbed ions. Many factors, such as heterogeneous mass transfer in electrolytes, inhomogeneous distribution of potential caused by different pore structures on electrode surface, and the variation in ionic concentration, will bring effects to the characteristics of double-layer structure. Consequently, the equivalent resistance and capacitance of the double-layer structure are not invariable, and they are both functions of operating frequency and working temperature [9]. Indeed, many electrochemical elements, such as ultracapacitors, batteries, and pseudocapacitors, are involved with these phenomena.

With the advancement of electrochemical testing technologies, fundamental works on the interaction behaviors of ions and different electrode materials have been emerging at a rate that has not been seen before in recent years [14–17]. As a consequence, the understanding about the double-layer structure is promoted and the electrochemical model is also being perfected. However, because of their complex forms and an invisible link to circuit elements, one can hardly find that electrochemical models are applied in the modeling and analyzing processes of circuit systems; instead, electronic and electrical engineers try to settle these issues in their own ways.

2.2 Equivalent impedance models

Usually, to streamline their normally cumbersome principles, the nominal value of a non-solid aluminum electrolytic capacitor is obtained by the manufacturers at 100/120 Hz and 20°C, to IEC 60384-4 standard [18]. However, circuit systems, such as power electronic regulators, can be designed to operate in a wide frequency band, so the nominal value may not give an accurate description on characteristics; the predicting errors will be inevitably brought in the process of design [19,20] and further result in the reduction in performances of the designed circuit systems [21]. Accordingly, a wide variety of equivalent circuit models are developed in academia and industry; Fig. 2 lists some typical ones:

Let us recall Fig. 1, in a non-solid electrolytic aluminum capacitor, metal materials are used as the terminal leads of electrodes, which always have finite electrical resistance and are connected in series with the double-layer structure, so that the simple R–C series model is adopted in many applications to reflect the ESR of the capacitor [14]. However, the R–C series model fails to reflect some characteristics of capacitors, so some more complex models are proposed then. In technical manuals provided by manufacturers Rubycon and TDK [6,18], the self-resonance phenomenon of capacitors under high operating frequency is considered, and an equivalent series inductance is added,

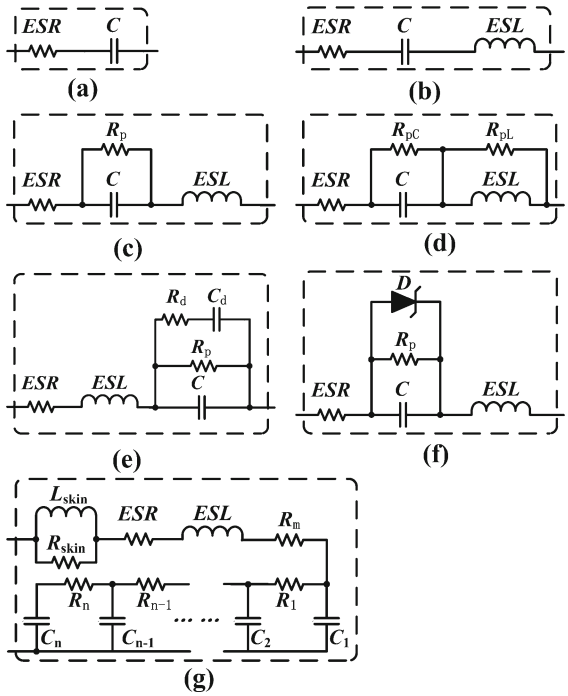

Fig. 2 Typical equivalent models of aluminum electrolytic capacitors: **a** *R–C* series model, **b** *R–C–L* series model, **c** Nichicon model, **d** leakage current model, **e** KEMET model, **f** Cornell Dubilier model, **g** Ladder network

but this model does not consider the effect of leakage current. Therefore, in the technical manual of the manufacturer Nichicon [5], the resistor R_p is added to the *R–C–L* model. For the same purpose, the authors of reference [22] use R_{pC} and R_{pL} to represent the effect of leakage current. These models of considering leakage current are adopted in the modeling and characteristic analysis of some circuit systems [23–25]. But beyond that, other factors which have effects on capacitor characteristics, such as the dielectric absorption and molecular polarization effects, cannot be neglected. In KEMET's model [26], a polarization resistor R_p, an absorption capacitor C_d, and a resistor R_d are parallel with the *R–C–L* model. Besides, to reflect the reverse voltage characteristic, Cornell Dublier's technical manual holds that Zener diodes need to be added to the equivalent circuit model [27]. In addition, some studies found that more complex ladder network models can be used to describe electrolytic capacitors, since the self-similar fractal structure of the electrode surface can be approximated by the series parallel impedance network [28].

One can see from the developing process of equivalent circuit models that the major objective of building a circuit model is to embody the actual electrical characteristics of capacitors. More numbers of elements in the model will bring a higher predicting precision, but a complex structure will cause inconvenience to the modeling and analysis of circuit systems.

2.3 Derivation of fractional-order impedance models

In recent years, the concept of fractional calculus arouses the interest of many scholars, although it is not a new topic in mathematics [29]. But it is worthwhile now to consider and study how to enrich the physical meaning and extend the application of fractional calculus. Indeed, many explorations on these issues have been presented in electronic and electrical engineering field [30–33], and in regards to the capacitors, in 1994, it was pointed out in reference [34] that the capacitor "remembers" voltages it has been subjected to earlier, which is evident from the definition of the fractional derivative. As a result, the concept of fractional impedance, or constant phase element (CPE), is introduced in the aforementioned works. The impedance of this kind of elements can be governed by the following equation:

$$\begin{aligned} Z &= \frac{1}{(j\omega)^{\alpha} C} \\ &= \frac{\cos\dfrac{\alpha\pi}{2}}{\omega^{\alpha} C} - j\frac{\sin\dfrac{\alpha\pi}{2}}{\omega^{\alpha} C}, \end{aligned} \tag{4}$$

in which $\omega = 2\pi f$ is the operating angular frequency and the order α corresponds to the relative dielectric permittivity of different materials and is relevant to the losses of the capacitor.

One can find that the impedance of the capacitor is divided into the real part and imaginary part, just like a resistor and a conventional capacitor which are in series with each other. Moreover, the above model shows that the impedance is a function of frequency, which can be associated with dielectric absorption. However, this model fails to accommodate the influence from manufacturing processes, as mentioned in its appendix, so the model would lead to inaccurate results when dealing with the actual situation. In reference [9], the authors suggest that the capacitor's fractional behaviors are mainly caused by the electrochemical materials of electrolyte, but not the terminal capacitor, and their model is shown in Fig. 3.

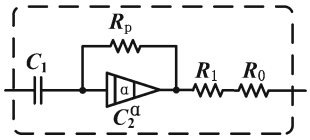

Fig. 3 A FO model of non-solid aluminum electrolytic capacitor in reference [9]

In the above model, the resistors R_0 and R_1 are used to represent the total resistance of electrolyte, foil, tabs, and terminal leads. C_1 is the terminal capacitance, R_2 is the dielectric loss of resistance, and C_2 is the dielectric loss capacitance, which has an order α. The impedance of the above FO equivalent circuit is:

$$\begin{aligned} Z &= \frac{1}{j\omega C_1} + R_0 + R_1 + R_p // \frac{1}{(j\omega)^\alpha C_2} \\ &= \frac{1}{j\omega C_1} + R_0 + R_1 \\ &\quad + \frac{R_p\left(1+\omega^\alpha R_p C_2 \cos\frac{\alpha\pi}{2}\right)}{1+\omega^{2\alpha}R_p^2C_2^2+2\omega^\alpha R_pC_2\cos\frac{\alpha\pi}{2}} \\ &\quad - \frac{j\omega^2 R_p^2 C_2 \sin\frac{\alpha\pi}{2}}{1+\omega^{2\alpha}R_p^2C_2^2+2\omega^\alpha R_pC_2\cos\frac{\alpha\pi}{2}}. \end{aligned} \tag{5}$$

In Eq. (5), the symbol "//" is used to represent the parallel connection between R_p and C_2^α. By Eq. (5), one can deduce the expressions for the equivalent capacitance,

$$\frac{1}{C_{\text{eq}}} = \frac{1}{C_1} + \frac{\omega^{1+\alpha}R_p^2C_2\sin\frac{\alpha\pi}{2}}{1+\omega^{2\alpha}R_p^2C_2^2+2\omega^\alpha R_pC_2\cos\frac{\alpha\pi}{2}} \tag{6}$$

and

$$\begin{aligned} \text{ESR} &= R_0 + R_1 \\ &\quad + \frac{R_p\left(1+\omega^\alpha R_pC_2\cos\frac{\alpha\pi}{2}\right)}{1+\omega^{2\alpha}R_p^2C_2^2+2\omega^\alpha R_pC_2\cos\frac{\alpha\pi}{2}}, \end{aligned} \tag{7}$$

respectively.

The above two FO models, especially the first one, are mainly based on Curie's empirical law about the current through a capacitor and an approximation of the impedance. In fact, to describe the electrochemical reactions on the surface of electrodes, scholars have developed the technique of electrochemical impedance spectroscopy (EIS) [35], which has been used to built the equivalent circuit models of batteries and ultracapacitors [36–41], and the concept of CPE, or fractional-order impedance, is widely adopted in equivalent circuit models obtained by EIS technique.

Fig. 4 Dual FOE model of non-solid aluminum electrolytic capacitor

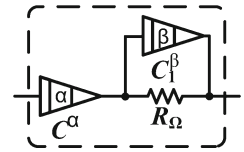

For the subject investigated in this work, non-solid aluminum electrolytic capacitor, the authors suggest that the equivalent model should consider not only the dielectric absorption of electrolyte but also the infinite self-similar structure of electrode surface, since it has an obvious effect on the surface area and arrangement of ions. Moreover, according to the distribution, most ions are located in the Helmholtz layer, so the characteristics of an electrolytic capacitor are dominated by the characteristics of this layer. Besides, the self-resonance phenomenon of electrolytic capacitors usually appears in frequency band that is higher than 1 MHz, in which the capacitance significantly reduces and the capacitors outlive their energy storage or filtering purposes. Therefore, a new equivalent model with two fractional-order elements (FOE) is proposed (Fig. 4).

The impedance of the above model is:

$$\begin{aligned} Z &= \frac{1}{(j\omega)^\alpha C} + R_\Omega // \frac{1}{(j\omega)^\beta C_1} \\ &= \frac{\cos\frac{\alpha\pi}{2} - j\sin\frac{\alpha\pi}{2}}{\omega^\alpha C} \\ &\quad + \frac{R_\Omega + \omega^\beta R_\Omega^2 C_1 \cos\frac{\beta\pi}{2}}{1+\omega^{2\beta}R_\Omega^2C_1^2+2\omega^\beta R_\Omega C_1\cos\frac{\beta\pi}{2}} \\ &\quad - j\frac{\omega^\beta R_\Omega^2 C_1 \sin\frac{\beta\pi}{2}}{1+\omega^{2\beta}R_\Omega^2C_1^2+2\omega^\beta R_\Omega C_1\cos\frac{\beta\pi}{2}}. \end{aligned} \tag{8}$$

By the above model, one can deduce the expression for the equivalent capacitance,

$$\frac{1}{C_{\text{eq}}} = \frac{\sin\frac{\alpha\pi}{2}}{\omega^{\alpha-1}C} + \frac{\omega^{1+\beta}R_\Omega^2C_1\sin\frac{\beta\pi}{2}}{1+\omega^{2\beta}R_\Omega^2C_1^2+2\omega^\beta R_\Omega C_1\cos\frac{\beta\pi}{2}}, \tag{9}$$

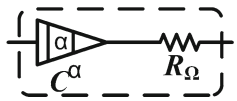

Fig. 5 A simplified FO equivalent model of non-solid aluminum electrolytic capacitor

and ESR,

$$\mathrm{ESR} = \frac{\cos\frac{\alpha\pi}{2}}{\omega^\alpha C} + \frac{R_\Omega + \omega^\beta R_\Omega^2 C_1 \sin\frac{\beta\pi}{2}}{1 + \omega^{2\beta} R_\Omega^2 C_1^2 + 2\omega^\beta R_\Omega C_1 \cos\frac{\beta\pi}{2}}, \tag{10}$$

respectively.

The surface of electrodes has an infinite self-similar fractal structure, the variations in current and electric potential have dispersion effects of time constant, and the constant phase element (CPE), or a fractional-order capacitor C^α, can be employed to describe this kind of effects [35]. At the same time, the influences of ions in electrolyte can be represented by a fractional-order capacitor C_1^β and a resistor R_Ω, like those in [9]. Note that there is a close correspondence between the proposed model (9) and the double-layer model (3). More specifically, the two models have a similar form, the first term of Eq. (9) corresponds to the Helmholtz capacitor, while the second term is related to the diffuse capacitor. The two parts of double-layer model (3) have the term ε_r, which is intrinsically related to the operating angular frequency ω. This trait can be reflected by the proposed model (9) in functions of ω.

The proposed dual FOE model constructs an invisible link between electrochemical principles and circuit elements; nevertheless, the authors hold that a simpler structure is preferred, since it would bring convenience to the modeling and analyzing processes of circuit systems. Accordingly, a simplified equivalent model is brought forward (Fig. 5).

The impedance of the above model is:

$$Z = \frac{1}{(j\omega)^\alpha C} + R_\Omega = \left(R_\Omega + \frac{\cos\frac{\alpha\pi}{2}}{\omega^\alpha C}\right) - j\frac{\sin\frac{\alpha\pi}{2}}{\omega^\alpha C}. \tag{11}$$

Then, one can deduce the expression for the equivalent capacitance,

$$C_{\mathrm{eq}} = \frac{\omega^{\alpha-1} C}{\sin\frac{\alpha\pi}{2}}, \tag{12}$$

and ESR,

$$\mathrm{ESR} = R_\Omega + \frac{\cos\frac{\alpha\pi}{2}}{\omega^\alpha C}, \tag{13}$$

respectively.

One can find that all the FO equivalent models show the frequency-related characteristic of the capacitor; additionally, the expressions for capacitance of the model in [9] and the proposed dual FOE model have a similar form with electrochemical double-layer model. To assess the predicting performance of these models, the subspace parameter estimating issue emerges.

3 Subspace parameter estimation

In traditional works for subspace parameters and state-of-charge (SOC) estimation of electrochemical elements, such as ultracapacitors [42], the recursive least squares (RLS)-based techniques are preferred. However, as to the optimization problem for FO models of this work, RLS-based techniques are not that effective, since the expressions for these objects cannot be expressed into the linear iteration form of parameter vector multiplies state variables, even without considering the influences of stochastic perturbation. As a result, a different approach should be developed; actually, this issue has aroused concerns in recent publications [43,44], but in these works, they are dealing with single objective problems. For the models in this work, just predicting the impedance or capacitance is not enough. Accordingly, a multi-objective estimating scheme is offered in the following subsection.

3.1 Implementation scenario of parameter estimation

On the basis of data obtained by an impedance analyzer (Wayne Kerr WK65120B), the problem of estimating the parameters of FO models is transformed into the problem of searching for global minimum of errors between measured data and predicting results of the models. The mean square error (MSE) between measured data and predicting results is adopted to describe the problem. Additionally, as it is known that the impedance consists of real and imaginary part, just like a capacitor which is in series with a resistor. This means that if any two of the impedance, capacitance, and ESR are determined, the rest one can be obtained at

the same time. Thus, the parameters estimated should guarantee that the MSE of impedance,

$$\mathrm{MSE}_1 = \frac{\sum_{k=1}^{N}[|Z(\omega_k)| - |Z_o(\omega_k)|]^2}{N}, \tag{14}$$

and the MSE of ESR

$$\mathrm{MSE}_2 = \frac{\sum_{k=1}^{N}[E(\omega_k) - E_o(\omega_k)]^2}{N}, \tag{15}$$

will have global minimum values at the same time, where the terms $E_o(\omega_k)$ and $|Z_o(\omega_k)|$ stand for the objective ESR and modules of impedance at the k^{th} operating angular frequency point, respectively. Consequently, one would face a optimization problem in the following work, and the objects are models mentioned in Sect. 2.

To minimize the values of Eqs. 14 and 15 simultaneously, the model parameters θ and the latent weight variable $\lambda = [\lambda_1, ..., \lambda_i]$ are jointly learned by minimizing:

$$\min_{\omega,\theta} E(\omega_{1...N}, \theta) = \sum_{i=1}^{2} \lambda_i \mathrm{MSE}_i(\omega_{1...N}, \theta). \tag{16}$$

As it shows, the above optimization problem is characterized by nonlinear, partially non-differentiable function; one should find a set of parameters which minimize the value of the above equation in the parameter space θ, which is constrained. In this subsection, different evolutionary (DE) algorithm is applied; it is a derivative-free optimization method, which was first used to solve Chebyshev's polynomial problem, and extended to solve optimization problems of complex systems [45]. This algorithm shows strong robustness and good convergence in dealing with multi-objective optimization problem [46]. The procedures of applying DE algorithm to FO models are shown in Fig. 6. Considering the number of elements in the parameter space to be predicted, the population size of the algorithm is selected to be 10 times of the number of parameters. The scaling factor of mutation operation and probability of crossover operation are selected as 0.85 and 0.8, respectively. Meanwhile, the DE/rand-to-best/1 strategy is selected. The latent weight variable λ is set to be [0.5, 0.5] since the two factors of Eq. (16) are of equal importance. Moreover, to prevent the parameter vectors from jumping out of the predetermined parameter space in the steps of mutation and crossover, a parameter restriction measure based on Bounce Back Strategy [47] is added in all steps.

3.2 Comparison between different models

In the work, the 50-V 10-μF Rubycon PX series capacitors are selected as the object to do technical verification. Moreover, to provide a reference, the KEMET model without equivalent series inductance is adopted; its impedance is:

$$\begin{aligned} Z &= R_\Omega + \frac{1}{j\omega C}//R_p//\left(\frac{1}{j\omega C_d} + R_d\right) \\ &= R_\Omega \\ &\quad + \frac{R_p(1-\omega^2 R_d C_d C R_p)}{(1-\omega^2 R_d C_d C R_p)^2 + \omega^2(R_p C + R_p C_d + R_d C_d)^2} \\ &\quad + \frac{\omega^2 R_d C_d R_p\left(R_p C + R_p C_d + R_d C_d\right)}{(1-\omega^2 R_d C_d C R_p)^2 + \omega^2(R_p C + R_p C_d + R_d C_d)^2} \\ &\quad + \frac{j\omega R_d C_d R_p(1-\omega^2 R_d C_d C R_p)}{(1-\omega^2 R_d C_d C R_p)^2 + \omega^2(R_p C + R_p C_d + R_d C_d)^2} \\ &\quad - \frac{j\omega R_p(R_p C + R_p C_d + R_d C_d)}{(1-\omega^2 R_d C_d C R_p)^2 + \omega^2(R_p C + R_p C_d + R_d C_d)^2}. \end{aligned} \tag{17}$$

Therefore, the subspace parameters of the four models awaiting identification are : $\theta_1 = [\alpha, R_\Omega]$, $\theta_2 = [\alpha, R_\Omega, \beta, C_1]$, $\theta_3 = [C_d, R_d, R_\Omega, R_p]$, and $\theta_4 = [\alpha, C_1, R_p, R_0 + R_1]$, respectively.

According to the above principles, and on the basis of a fixed nominal value of capacitance 10 μF, one can obtain that the subspace parameters of the above four models are: $\theta_1 = [0.985, 0.9629\ \Omega]$, $\theta_2 = [0.9883, 1.2430\ \Omega, 0.2808,\ 5\ \mathrm{mF}]$, $\theta_3 = [1\ \mu\mathrm{F}, 5.8041\ \mathrm{k}\Omega, 1.2543\ \Omega, 1.2173\ \mathrm{M}\Omega]$, and $\theta_4 = [0.7494,\ 4.5\ \mathrm{mF}, 6.0298\ \Omega, 0.9491\ \Omega]$, respectively. Then, one can draw the impedance values of the four models together in Fig. 7, and curves obtained by different models are enlarged in four different frequency ranges.

From Fig. 7, one can find out that all curves appear in exponential decline trend, and all these equivalent models can reflect the tendency of impedance with operating frequency. In frequency ranges of 100 Hz to 10 KHz, the differences between different curves are so small that it is hard to distinguish one another apart. However, along with the increase in frequency, the predicting error of integer-order KEMET model is rising. Additionally, the measured capacitance and ESR values are put together with those obtained by different equivalent models in Fig. 8. According to the results, one can find out that all these models can reflect the downward tendency of equivalent series resistance, especially in the frequency band larger than 1 kHz, which is the main

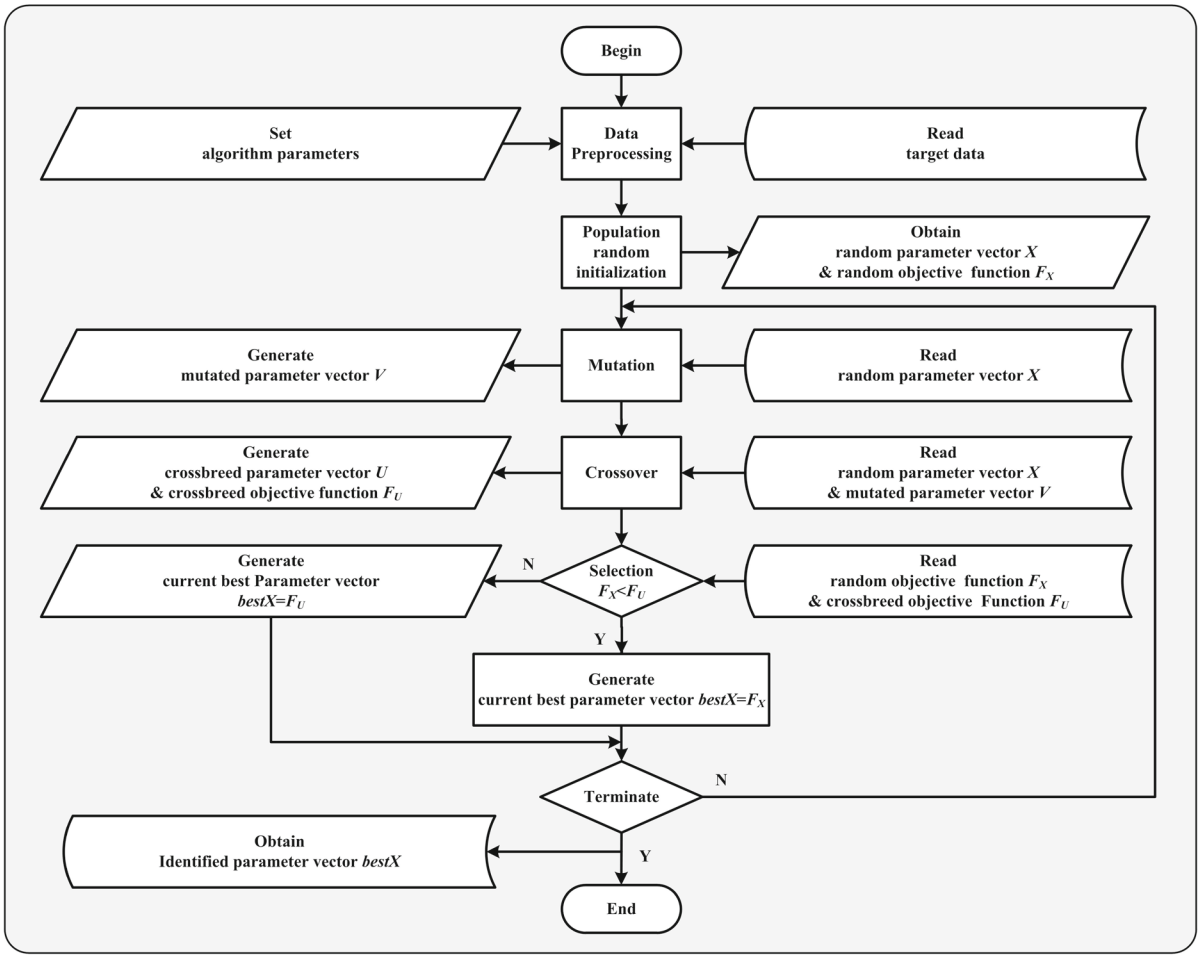

Fig. 6 Flowchart for offline parameter estimation of non-solid aluminum electrolytic capacitor based on DE

working band of modern power electronic equipments. Note that KEMET model can hardly reflect the variation in capacitance with working frequency, whereas three FO equivalent circuit models can reflect the downward trend of capacitance along with the increase in operating frequency, especially the dual FOE model.

Further, the relative errors Δe_x between measurements x and inferred results x_i are compared in Fig. 9, which is defined by

$$\Delta e_x = \frac{\delta e_x}{x} \times 100\%, \tag{18}$$

where δe_x is the absolute value between measurements and inferred values and the percentage error is 100% times the relative error.

One can find out that, in a wide frequency range, the proposed dual FOE model has the lowest relative errors of total impedance and capacitance, and in 0 Hz to 100 kHz, relative errors of impedance, ESR, and capacitance of the proposed dual FOE model are no more than 20%. Accordingly, the proposed dual FOE model can more closely reflect the frequency-related characteristics of non-solid aluminum electrolytic capacitors.

4 Output ripple analysis of DC–DC converters based on fractional-order models

As mentioned in introduction part, an inaccurate estimation for the capacitance and ESR of electrolytic capacitors will lead to an unreasonable design of the circuit system. For example, in DC–DC converters, electrolytic capacitors are always adopted to filter high-frequency components of the output voltage ripple; the capacitance and ESR are intrinsically related to

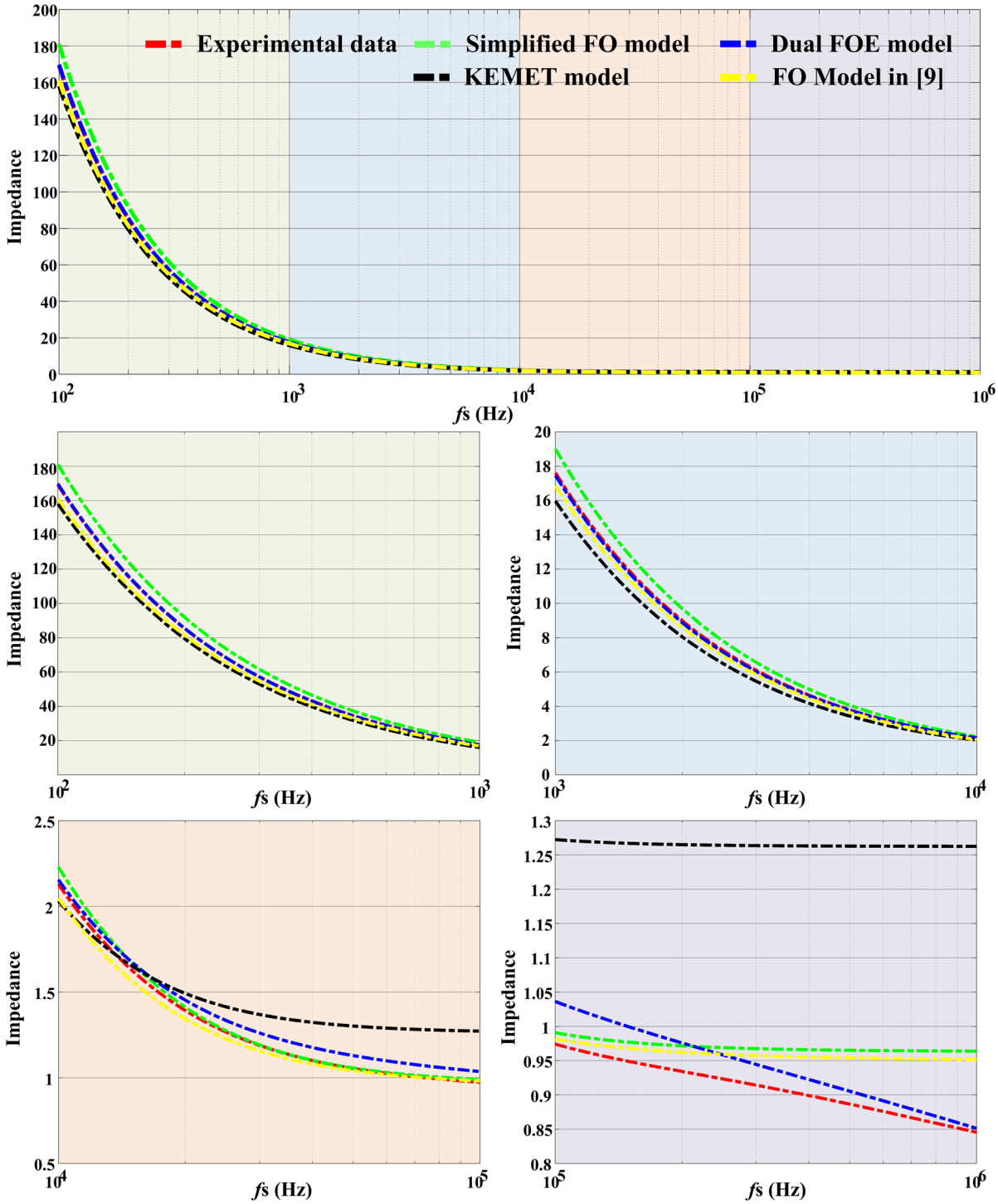

Fig. 7 Comparison between measured modules of impedance and predicting data obtained by different models

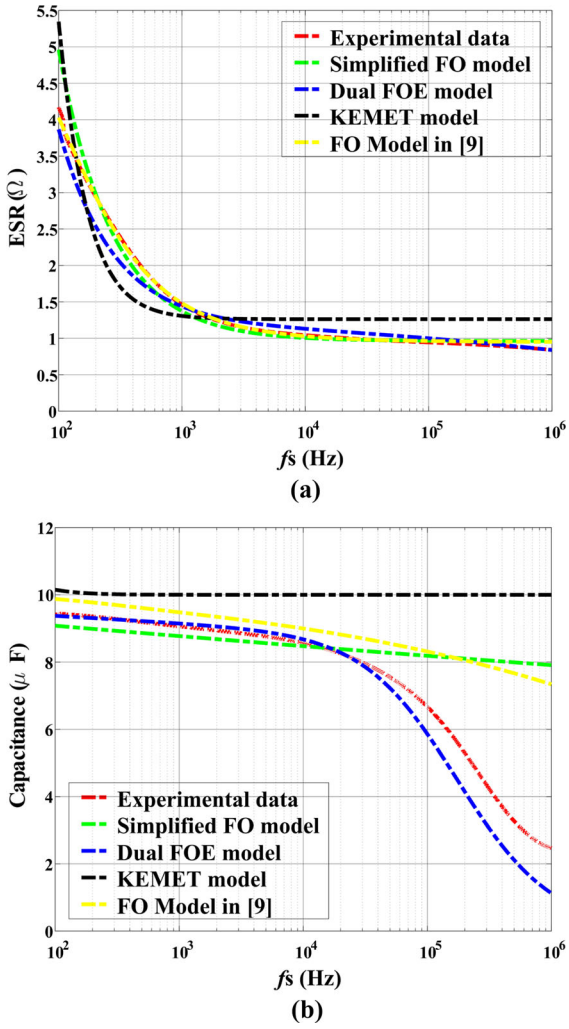

Fig. 8 Comparison between measured data and predicting data obtained by different models: **a** ESR, **b** capacitance

the shape of the ripple. It is certainly worth predicting the capacitance and ESR at a high precision; a concise description for the circuit topology is also necessary in the design and analyzing processes. Thus, one should seek balance between the above two aspects of demand.

4.1 Numerical simulation and experiments

Usually, non-solid aluminum electrolytic capacitors are applied in switching power supplies that are operated in [10 kHz, 100 kHz] frequency band. In Fig. 8, one can find that the predicting errors of the simplified FO model are no more than 20% for both capacitance and

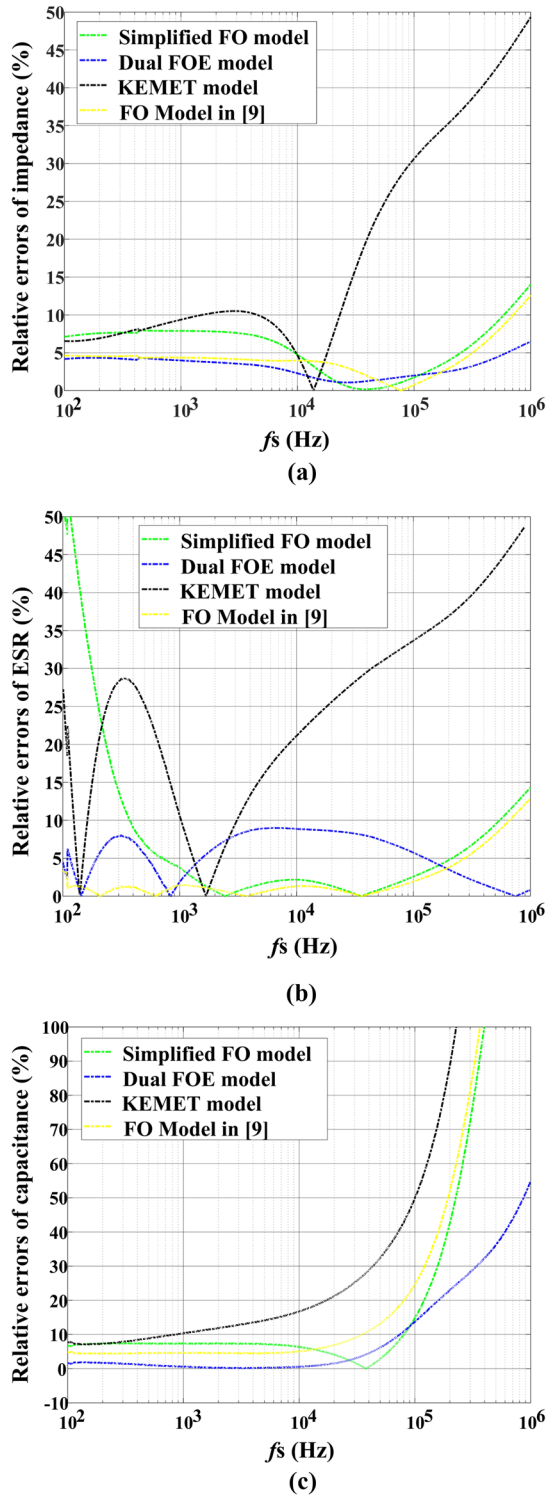

Fig. 9 Relative errors between measurements and different predicted results: **a** impedance, **b** ESR, **c** capacitance

ESR, so this model is adopted in a DC–DC Boost converter as an example like follows:

In the above Boost converter, the DC input voltage is set to be $V_{\text{in}} = 12$ V; the integrated shielding inductance $L = 100\ \mu$H is selected, which usually has a DC series resistance R_{LS}. The power switch S_T has a conduction resistance $R_{gs} = R_T$, and the switch-on duty ratio is 0.25. The power diode S_D has an instantaneous forward voltage V_{D}. A 10-μF non-solid aluminum capacitor is adopted as output filtering capacitor, and the resistance load $Z_L = R_o$ is about 10 Ω. Additionally, to sense the inductor current, a sensing resistance $R_{\text{sense}} = 20$ mΩ is adopted in the topology. The above parameters ensure the converter operates in continuous conduction mode (CCM) [48].

Taking the inductor current i_L and fractional capacitor voltage v_C as state variables, the state of the converter can be governed by the following equation when the switch S_T is on:

$$\frac{\mathrm{d}i_L}{\mathrm{d}t} = \frac{V_{\text{in}}}{L} - \frac{R_{\text{LS}} + R_T + R_{\text{sense}}}{L} i_L \tag{19a}$$

$$\frac{\mathrm{d}^\alpha v_C}{\mathrm{d}t^\alpha} = -\frac{v_C}{(R_o + R_\Omega)C} \tag{19b}$$

$$v_o = \frac{R_o v_C}{R_o + R_\Omega}. \tag{19c}$$

Otherwise, the state of the converter can be described by:

$$\frac{\mathrm{d}i_L}{\mathrm{d}t} = \frac{V_{\text{in}} - V_D}{L} - \frac{R_{\text{LS}} + R_{\text{sense}}}{L} i_L - \frac{R_o R_\Omega i_L}{(R_o + R_\Omega)L} - \frac{R_o v_C}{(R_o + R_\Omega)L} \tag{20a}$$

$$\frac{\mathrm{d}^\alpha v_C}{\mathrm{d}t^\alpha} = \frac{R_o i_L}{(R_o + R_\Omega)C} - \frac{v_C}{(R_o + R_\Omega)C} \tag{20b}$$

$$v_o = \frac{R_o v_C}{R_o + R_\Omega} + \frac{R_o R_\Omega i_L}{R_o + R_\Omega}. \tag{20c}$$

The converter flips forth and back between the above two states with the on and off actions of S_T, so it is a piecewise smooth fractional-order system. Thus, an Adams–Bashforth–Moulton (ABM) type numerical method can be applied to obtain its solutions [49], like those simulation works in reference [33]. Then, a comparison of the simplified FO model, conventional R–C series model, and ideal capacitor model under different switching frequencies can be performed. In simulations, the nominal capacitance is used in all three models to simplify the analysis process, since engineers usually measure capacitance with multimeter, which uses NE555 circuit to generate sinusoidal signals of about 80–800 Hz; in this frequency range, the capacitance does not deviate from nominal value very much. ESR value of the R–C series model is set according to the dissipation factor in manuals, that is:

$$\text{ESR} = \frac{\tan\delta}{2\pi f C}, \tag{21}$$

so that ESR can be calculated according to impedance angle, operating frequency, and capacitance, but both ESR and capacitance are constant in R–C series model. Moreover, the order $\alpha = 0.985$ is adopted in the simplified fractional-order model.

When the switching frequency is 20 kHz, 50 kHz, and 100 kHz, respectively, one can see the comparison results in Fig. 11, where black solid lines represent PSIM simulation with ideal capacitors, blue dash–dot lines come from PSIM simulation with R–C series models of capacitors, and those red dash–dot lines are from numerical simulation with simplified FO model of capacitors.

In these figures, one can find an obvious difference between waveforms obtained by different models. There are minute differences between those with ideal capacitors and R–C series models, especially those with ideal capacitors, the shape of output voltage just like classical descriptions in textbooks. However, there are obvious distortions in waveforms with simplified FO model of capacitors; specifically, at the moments of switch-on events, there are rapid changes in output voltage (Fig. 10).

From Fig. 11, one can see that the differences of output voltage grow with the increase in switching frequency. These differences are awaiting to be further distinguished, so experimental works are considered. In experiments, the type of power switch S_T is STP80NF70, which has a maximum conduction resistance $R_{gs} = R_T = 10$ mΩ, and is driven by a piece of Si8271 isolator. The power diode S_{D} is MUR1620, the maximum instantaneous forward voltage V_{D} of which

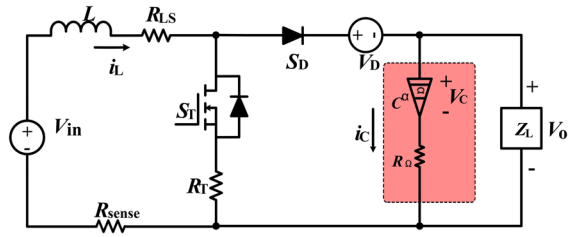

Fig. 10 DC–DC Boost converter with fractional capacitor model

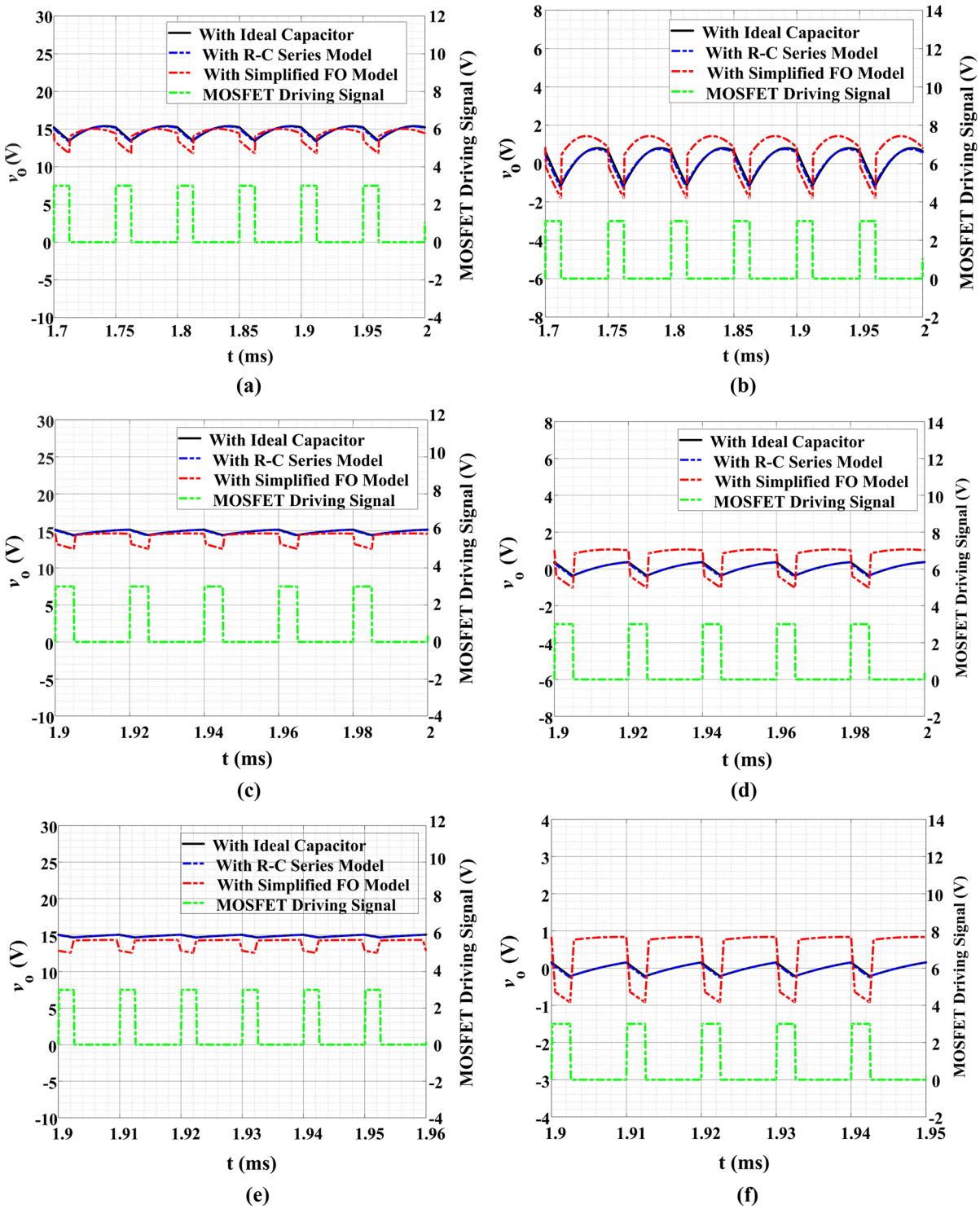

Fig. 11 Comparison of output voltage under different operating frequencies: **a** steady-state output voltage at 20 kHz, **b** ripples of output voltage Δv_o at 20 kHz, **c** steady-state output voltage at 50 kHz, **d** ripples of output voltage Δv_o at 50 kHz, **e** steady-state output voltage at 100 kHz, **f** ripples of output voltage Δv_o at 100 kHz

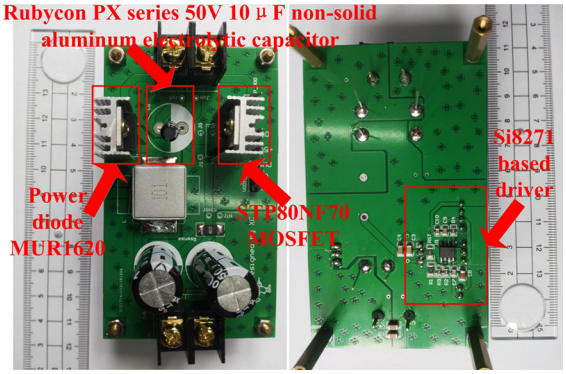

Fig. 12 Photograph of test bench

is no more than $1.05V$. The inductor L has a maximum DC series resistance $R_{\mathrm{LS}} = 4\,\mathrm{m}\Omega$ according to manuals. A C = 10-μF Rubycon PX 50-V series non-solid aluminum capacitors is adopted to smooth the output voltage, which has a dissipation factor of $\tan\delta = 0.12$ [50]. Then, a test bench is constructed as follows (Fig. 12).

By adopting the above test bench, driving signals and output voltage are captured by an oscilloscope, as shown in Fig. 13. In all subfigures, steady-state output voltage v_o, ripples of the voltage Δv_o, and MOSFET driving signals (orange solid lines) from a signal generator are captured. From this figure, one can find that there are also rapid changes in output voltage at the switch-on time in experiments. Moreover, the magnitudes of voltage ripples decrease with the operating frequency, just like the numerical simulation shows. Furthermore, the peak-to-peak values of output voltage from both experiments and numerical simulation based on ABM method are listed in Table 1.

Considering parasitic parameters, such as parasitic resistance of the circuit, the maximum instantaneous forward voltage of the MOSTFET, and the maximum conduction impedance of the diode, the errors between experimental results and numerical simulations based on simplified FO models of non-solid aluminum electrolytic capacitors are almost the same, yet there is a great error in those with traditional models. The comparisons confirm the superiority of applying FO techniques in ripple analysis of DC–DC converters.

4.2 Discussion

One can find in Sect. 4.1 the shapes of the modeled output voltage waveforms (Fig. 11) differ significantly from those experimental waveforms (Fig. 13), especially with high switching frequencies. One may wonder that this phenomenon is caused by Miller effect or other similar phenomena of power MOSFET; these phenomena will lead to distortions of waveforms between gate and source of power MOSFET. In the process of making PCB boards, we considered the possible existence of Miller effect and tried to eliminate the impacts as much as possible, where we selected a type STP80NF70 power MOSFET as power switch, the gate charge Q_{g} of which is very low, which is about 70 nC. Moreover, the driving IC is placed as close as possible to the gate pin of power MOSFET. Thus, in experiments, we can hardly find Miller plateau during switch-on processes of the MOSFET. Moreover, we tried to build yet another two PCB boards to do comparison by adopting two different MOSFET power switches, IRF640B and FQPF5N60C, the gate charge Qg of which is 64 nC and 15 nC on datasheets, respectively. By comparison, we find that the experimental results are almost the same, the duty ratio of experimental voltage between drain and source of switch transistor is 25%, which equals to the driving signal. Thus, it can be confirmed that Miller effect is not the main reasons that cause the differences between voltage waveforms of Figs. 11 and 13.

Then, it is found out that the reverse recovery characteristics of power diodes have obvious impacts on the experimental waveforms (Fig. 13). In different PCB boards, ultrafast diode MUR1620CT and hyperfast diode RHRH3060 are adopted, the maximum reverse recovery time of which is 60 ns and 40 ns in datasheets, respectively. However, experimental results show that the electrical characteristics of power diodes are not that ideal, and switching-on actions of these diodes are not as fast as those listed in datasheets. Some typical waveforms obtained in experiments are attached as shown in Fig. 14, where green curves represent voltage between cathode and anode of power diode, blue curves are those of voltage between gate and source of power MOSFET, and orange curves belong to the output voltage of Boost converter. One can see that, at the falling edge time of power MOSFET, the power diode is not fully conducted, power diode voltage climbs slowly, thus the electrolytic capacitor is still in discharging state, and the output voltage of the converter keeps falling in this period of time, which is about 2 to 4 μs, as the experimental waveforms reflected. After the above

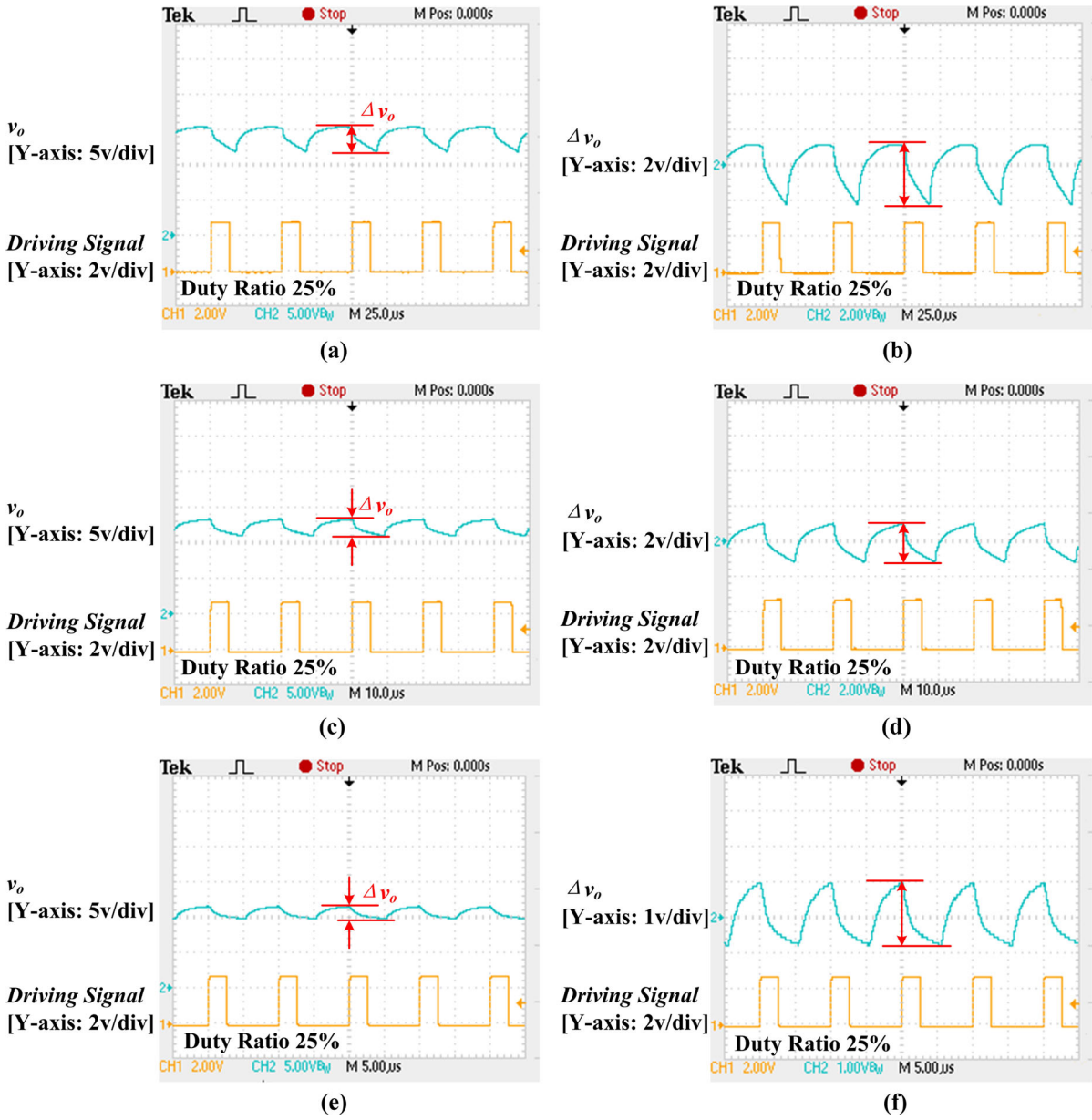

Fig. 13 Waveforms obtained in experiments: **a** steady-state output voltage at 20 kHz, **b** ripples of output voltage Δv_o at 20 kHz, **c** steady-state output voltage at 50 kHz, **d** ripples of output voltage Δv_o at 50 kHz, **e** steady-state output voltage at 100 kHz, **f** ripples of output voltage Δv_o at 100 kHz

process, the power diode is fully conducted, with about 1 volt forward voltage.

According to the analysis above, an equivalent circuit of the Boost converter with considering parasitic parameters of power diode can be adopted to represent this period of time, as shown in Fig. 15, and like that of [51], the dash lines represent that these branches are not conducted, and a junction capacitor C_D is added to the equivalent circuit. According to sneak circuits of the converter, the junction capacitor C_D hinders a rapid voltage change between cathode and anode of power diode. As a result, there is a period of time, during which

Table 1 Comparison of peak-to-peak ripples Δv_o obtained by numerical simulations and experiments

	20 kHz	50 kHz	100 kHz
Experiments	3.57	2.20	1.81
With ideal capacitor	1.95	0.74	0.37
With R–C series model	2.11	0.80	0.41
With simplified FO model	3.26	2.09	1.76

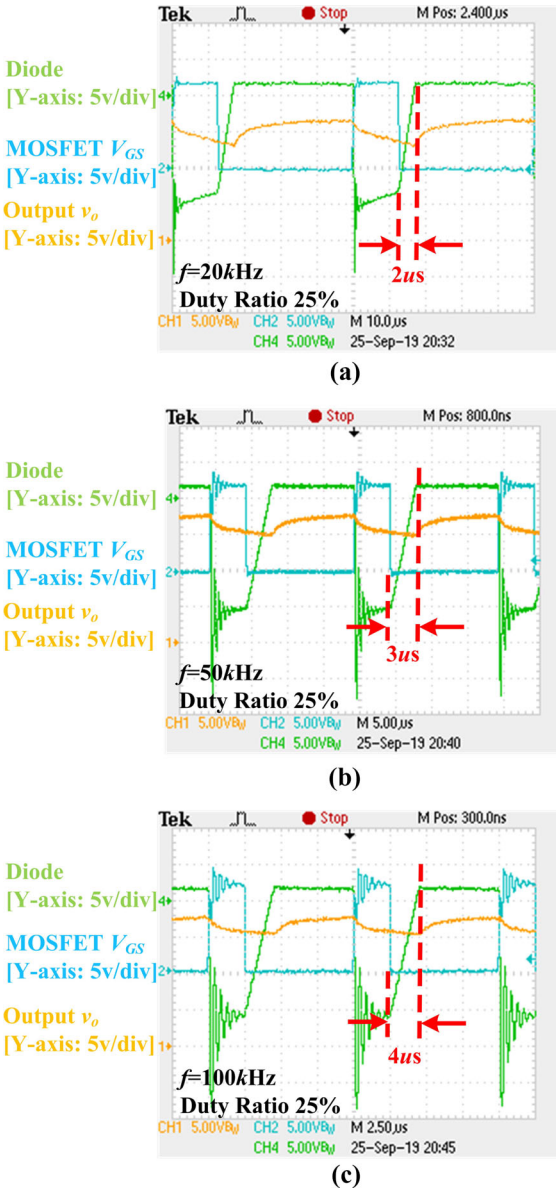

Fig. 14 Enlarged experimental waveforms: **a** $f = 20$ kHz, **b** $f = 50$ kHz, **c** $f = 100$ kHz

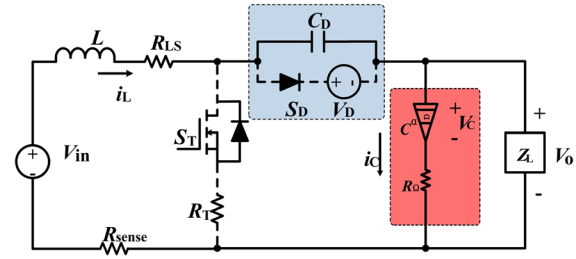

Fig. 15 DC–DC Boost converter considering parasitic parameters of power diode

the output filtering capacitor is still in discharging state, and there is a continuing decline in the output voltage. It is thus clear that the unsatisfactory reverse recovery characteristics of power diodes lead to the difference between the modeled output voltage waveforms in Fig. 11 and the experimental waveforms in Fig. 13. Accordingly, frequency-dependent phenomena in both active and passive devices, influences of parasitic elements, are issues worthy of in-depth exploration in further works.

5 Conclusions

The performance and reliability of power electronic equipments attract high concerns in applications, which have a lot to do with the parameter condition of components such as capacitors. In this work, the frequency-dependent parameter shift of non-solid aluminum electrolytic capacitors is studied, two fractional-order equivalent circuit models are proposed, and an error optimization scheme based on differential evolution algorithm is presented for parameter identification of the two proposed models. Comparisons show that the two proposed fractional-order models can reflect the frequency-dependent characteristics of both impedance and ESR in high accuracy in a wide operating frequency range, and they can predict the downward trend of capacitance along with the increase in operating frequency, where the proposed dual FOE model has the highest predicting accuracy, since the dual FOE structure corresponds to the double-layer structure of electrolytic capacitors. Moreover, one of the proposed fractional equivalent models, the simplified fractional-order model, is adopted in the output voltage ripple analysis of an open-looped DC–DC boost converter, in which a non-solid aluminum electrolytic capacitor

is employed as the output filtering capacitor. Numerical calculating results and experiments show that theoretical analysis results of those obtained by the proposed fractional-order model have a higher accuracy than those with traditional ideal capacitor model and the R-C series model. Therefore, utilizing fractional-order models and techniques will help to provide more effective guidance for real circuit design and performance assessment.

Compliance with ethical standards

Conflict of interest The authors declare that they have no conflict of interest.

References

1. Yang, S., Bryant, A., Mawby, P., Xiang, D., Ran, L., Tavner, P.: An industry-based survey of reliability in power electronic converters. IEEE Trans. Ind. Appl. **47**(3), 1441–1451 (2011)
2. Zhu, B., Zeng, Q., Chen, Y., Zhao, Y., Liu, S.: A dual input high step Up DC–DC converter with ZVT auxiliary circuit. IEEE Trans. Energy Convers. **34**(1), 161–169 (2019)
3. Xi, L., Chen, J., Huang, Y., Yanchun, X., Liu, L., Zhou, Y., Li, Y.: Smart generation control based on multi-agent reinforcement learning with the idea of the time tunnel. Energy **153**, 977–987 (2018)
4. Both, J.: The modern era of aluminum electrolytic capacitors. IEEE Electr. Insul. Mag. **31**(4), 24–34 (2015)
5. Nichicon: General description of aluminum electrolytic capacitors. [Online]. https://www.nichicon.co.jp/english/products/pdf/aluminum.pdf. Accessed Apr 2017
6. Rubycon: Manufacture of alumunim electrolytic capacitor. [Online]. http://www.rubycon.co.jp/de/products/alumi/pdf/Process.pdf. Accessed Sept 2017
7. Bard, A.J., Faulkner, L.R., Methods, E.: Fundamentals and Applications, 2nd edn. Wiley, New York (2000)
8. Imam, A.M.: Condition monitoring of electrolytic capacitors for power electronics applications. Ph.D. dissertation, Georgia Institute of Technology (2007)
9. Malek, H., Dadras, S., Chen, Y.: Fractional order equivalent series resistance modeling of electrolytic capacitor and fractional order failure prediction with application to predictive maintenance. IET Power Electron. **9**(8), 1608–1613 (2016)
10. Cheng, K.-Y., Yu, F., Lee, F.C., Mattavelli, P.: Digital enhanced V^2-type constant on-time control using inductor current ramp estimation for a buck converter with low-ESR capacitors. IEEE Trans. Power Electron. **28**(3), 1241–1252 (2013)
11. Sundararajan, P., Sathik, M.H.M., Sasongko, F., Tan, C.S., Tariq, M., Simanjorang, R.: Online condition monitoring system for DC-link capacitor in industrial power converters. IEEE Trans. Ind. Appl. **54**(5), 4775–4785 (2018)
12. Hammam Soliman, H., Blaabjerg, W.F.: A review of the condition monitoring of capacitors in power electronics converters. IEEE Trans. Ind. Appl. **52**(6), 4976–4989 (2016)
13. Xu, N., Riley, J.: Nonlinear analysis of a classical system: the double-layer capacitor. Electrochem. Commun. **13**(10), 1077–1081 (2011)
14. Simon, P., Gogotsi, Y., Dunn, B.: Where do batteries end and supercapacitors begin? Science **343**, 1210–1211 (2014)
15. Costentin, C., Porter, T.R., Savéant, J.-M.: How do pseudocapacitors store energy? Theoretical analysis and experimental illustration. ACS Appl. Mater. Interfaces **9**(10), 8649–8658 (2017)
16. Forse, A.C., Merlet, C., Griffin, J.M., Grey, C.P., Savéant, J.-M.: How do pseudocapacitors store energy? Theoretical analysis and experimental illustration. J. Am. Chem. Soc. **138**(18), 5731–5744 (2016)
17. Prehal, C., Koczwara, C., et al.: Quantification of ion confinement and desolvation in nanoporous carbon supercapacitors with modelling and in situ X-ray scattering. Nat. Energy **2**(3), 16215 (2017)
18. TDK: Aluminum electrolytic capacitors: general technical information. [Online] (2017). https://www.tdk-electronics.tdk.com/download/530704/5f33d2619fa73419e2a4af562122e90c/pdf-generaltechnicalinformation.pdf. Accessed July 2018
19. Cheng, K.Y., Yu, F., Mattavelli, P., Lee, F.C.: Digital enhanced V2-type constant on-time control using inductor current ramp estimator for a buck converter with small ESR capacitors. In: 2010 IEEE Energy Conversion Congress and Exposition, Atlanta, GA, pp. 508–513 (2010)
20. Leyva-Ramos, J., Ortiz-Lopez, M.G., Diaz-Saldierna, L.H.: The effect of ESR of the capacitors on modeling of a quadratic boost converter. In: 2008 11th Workshop on Control and Modeling for Power Electronics, Zurich, pp. 1–5 (2008)
21. Bao, B.C., Yang, J., Xu, J.P., Zhang, X., Zhou, G.H.: Effect of output capacitor ESR on dynamic performance of voltage-mode hysteretic controlled buck converter. Electron. Lett. **49**(20), 1293–1294 (2013)
22. Braham, A., Lahyani, A., Venet, P., Rejeb, N.: Recent developments in fault detection and power loss estimation of electrolytic capacitors. IEEE Trans. Power Electron. **25**(1), 33–43 (2010)
23. Abdennadher, K., Venet, P., Rojat, G., Retif, J.-M., Rosset, C.: A real-time predictive-maintenance system of aluminum electrolytic capacitors used in uninterrupted power supplies. IEEE Trans. Ind. Appl. **46**(4), 1644–1652 (2010)
24. Zhao, K., Ciufo, P., Perera, S.: Rectifier capacitor filter stress analysis when subject to regular voltage fluctuations. IEEE Trans. Power Electron. **28**(7), 3627–3635 (2013)
25. Kieferndorf, F.D., Forster, M., Lipo, T.A.: Reduction of DC-bus capacitor ripple current with PAM/PWM converter. IEEE Trans. Ind. Appl. **4**(2), 607–614 (2004)
26. KEMET: Surface mount capacitors. [Online]. http://www.dialelectrolux.ru/files/file/Kemet/f3102.pdf. Accessed July 2018
27. CDM Cornell Dubilier: Aluminum electrolytic capacitor application guide. [Online]. http://www.cde.com/resources/catalogs/AEappGUIDE.pdf. Accessed July 2018
28. Parler, S.G.: Improved spice models of aluminum electrolytic capacitors for inverter applications. IEEE Trans. Ind. Appl. **39**(4), 929–935 (2003)
29. Podlubny, I.: Fractional Differential Equations. Academic Press, London (1998)

30. Elwakil, A.S.: Fractional-order circuits and systems: an emerging interdisciplinary research area. IEEE Circuits Syst. Mag. **10**(4), 40–50 (2010)
31. Petráš, I.: Fractional-Order Nonlinear Systems. Springer, Berlin (2011)
32. Si, G., Zhu, J., Diao, L., Ding, Z.: Modeling, nonlinear dynamic analysis and control of fractional PMSG of wind turbine. Nonlinear Dyn. **88**, 1608–1613 (2016)
33. Chen, X., Chen, Y., Zhang, B., Qiu, D.: A modeling and analysis method for fractional-order DC–DC converters. IEEE Trans. Power Electron. **32**(9), 7034–7044 (2017)
34. Westerlund, S., Ekstam, L.: Capacitor theory. IEEE Trans. Dielectr. Electr. Insul. **1**(5), 826–839 (1994)
35. Mark, E.: Orazem Bernard Tribollet, Electrochemical Impedance Spectroscopy, Chapter 13: Time-Constant Dispersion. Wiley, London (2008)
36. Sabatier, J., Cugnet, M., Laruelle, S., Grugeon, S., Sahut, B., Oustaloup, A., Tarascon, J.M.: A fractional order model for lead-acid battery crankability estimation. Commun. Nonlinear Sci. Numer. Simul. **15**(5), 1308–1317 (2010)
37. Jun, X., Mi, C., Cao, B., Cao, J.: A new method to estimate the state of charge of lithium-ion batteries based on the battery impedance model. J. Power Sources **233**, 277–284 (2013)
38. Wang, B., Liu, Z., Li, S.E., Moura, S.J., Peng, H.: Fractional modeling and SOC estimation of lithium-ion battery. IEEE Trans. Control Syst. Technol. **25**(1), 3–11 (2017)
39. Hao, M., Xiong, R., Zheng, H., Chang, Y., Chen, Z.: A novel fractional order model based state-of-charge estimation method for lithium-ion battery. Appl. Energy **207**, 384–393 (2017)
40. Bertrand, N., Sabatier, J., Briat, O., Vinassa, J.M.: Embedded fractional nonlinear supercapacitor model and its parametric estimation method. IEEE Trans. Ind. Electron. **57**(12), 3991–4000 (2010)
41. Kumar, M.R., Ghosh, S., Das, S.: Frequency dependent piecewise fractional-order modelling of ultracapacitors using hybrid optimization and fuzzy clustering. J. Power Sources **335**, 98–104 (2016)
42. Reichbach, N., Kuperman, A.: Recursive-least-squares-based real-time estimation of supercapacitor parameters. IEEE Trans. Energy Convers. **31**(2), 810–812 (2016)
43. Leyden, K., Goodwine, B.: Fractional-order system indentificaiton for health monitoring. Nonlinear Dyn. **92**, 1317–1334 (2018)
44. Allafi, W., Zajic, I., Uddin, K., Shen, Z., Marco, J., Burnham, K.: Design of delayed fractional state variable filter for parameter estimation of fractional nonlinear models. Nonlinear Dyn. **94**(4), 2697–2713 (2018)
45. Price, K.V., Storn, R.M., Lampinen, J.A., Evolution, D.: A Practical Approach to Global Optimization. Springer, Berlin (2005)
46. Wang, W., Yang, S., Lin, Q., Zhang, Q., Wong, K.-C., Coello, C.A.C., Chen, J.: An effective ensemble framework for multi-objective optimization. IEEE Trans. Evol. Comput. **23**(4), 645–659 (2019)
47. Coello, C.A.C.: Theoretical constraint-handling techniques used with evolutionary algorithms: a survey of the state of the art. Comput. Methods Appl. Mech. Eng. **191**(11), 1245–1287 (2002)
48. Erickson, R.W., Maksimovic, D.: Fundamentals of Power Electronics. Springer, New York (2001)
49. Diethelm, K., Ford, N., Freed, A.: A predictor–corrector approach for the numerical solution of fractional differential equations. Nonlinear Dyn. **29**, 3–22 (2002)
50. Rubycon: Radial lead aluminum electrolytic capacitors: PX series. [Online]. http://www.rubycon.co.jp/en/catalog/e_pdfs/aluminum/e_px.pdf. Accessed July 2018
51. Li, M., Zhang, B., Qiu, D., Zhang, G.: Sneak circuit phenomena in a DCM boost converter considering parasitic parameters. IEEE Trans. Power Electron. **32**(5), 3946–3958 (2017)